Planning the Perfect Burn: Multi-Objective PSO for Multi-Needle Thermal Ablation

Jonas Mehtali[1], Juan Manuel Verde[123], and Caroline Essert[1]

[1] ICube, University of Strasbourg, CNRS, France
[2] IHU Strasbourg - Institute of Image-Guided Surgery, France
[3] INRIA, Strasbourg, France
j.mehtali@unistra.fr

Abstract. Percutaneous thermal ablation is a localized treatment for hepatic tumors for which multi-needle planning remains mostly manual, while the difficulty grows sharply with the number of needles and the complexity of the targets. We present a GPU-accelerated pipeline that jointly optimizes all needle placements and ablation parameters in a single run, to aim for a perfect burn. Our pipeline uses a decomposition-based multi-objective particle swarm optimizer, with four clinical objectives (coverage, efficiency, safety, insertion depth), per-needle activation variables to optimize needle count, a CUDA-based fitness evaluation, and Vulkan-rendered safety maps. Tested on 94 tumors, the method achieves better coverage, larger distance to critical structures, and less collateral damage than the expert plan, in less than 6 seconds. An expert rated 88% of auto-plannings as clinically acceptable as is ($\geq$4/5) and 99% as requiring only minor adjustments ($\geq$3/5), with 97% judged equivalent or superior to manual plans (87% preferred, 10% equivalent).

Keywords: Thermal ablation · Treatment planning · Multi-objective optimization · GPU acceleration · Particle swarm optimization

1 Introduction

Percutaneous thermal ablation (PTA) is a first-line treatment for hepatic tumors [9,6] in which a needle-like applicator delivers thermal energy at its tip to induce localized tumor necrosis. Tumor recurrence depends critically on the *minimal ablation margin* (MAM), a 5–10 mm layer of destroyed tissue surrounding the tumor. Insufficient MAM is an independent predictor of recurrence [11]. For large or irregular tumors, multiple impacts, either through the same (pullback) or different applicators, may be needed to fully cover the margin. This complex combinatorial problem involves a dozen decision variables per needle, and the clinician must balance four conflicting objectives simultaneously. In practice, this time-consuming task is performed mentally with limited 3D spatial reasoning.

For more than two decades, the literature has addressed mostly parts of this problem. *Trajectory-only* methods [3,2,22,17] optimize single-needle insertion but ignore needle count, ablation parameters, and composite multi-needle coverage.

Sequential multi-needle methods [16,21,14] place needles in stages, preventing revision of earlier decisions and potentially leading to suboptimal composite plans. In the most recent study, Pan et al. [21] achieved automatic planning in 22 s using whale optimization with extensive clinical constraints, but predefined needle targets and ablation dimensions. Lukes et al. [17] jointly optimized multiple trajectories with adaptive needle count but fixed ablation geometry and relied on weighted-sum scalarization, which may overlook portions of the Pareto front [10]. *Simulation-based* methods [15] improve accuracy via thermal modeling but incur prohibitive computational cost (∼480 s on CPU [15]), precluding intraoperative replanning. *Learning-based* approaches [4,20] offer fast inference but remain limited to single needles or single targets. Recent surveys [23,8,27] confirmed that no existing method simultaneously provides: (a) joint optimization of all needles, (b) true multi-objective Pareto optimization across coverage, efficiency, safety, and depth, (c) adaptive needle count including pullback ablations, (d) safety-aware trajectory selection inside the optimization loop, and (e) speed compatible with intra-operative use.

We address these gaps with the following contributions:

1. GPU-accelerated 4-objective pipeline that **jointly** optimizes multi-needle trajectories, ablation parameters, and safety.
2. **MOEA/D–PSO formulation** yielding a clinically meaningful Pareto front.
3. **Per-needle activation encoding with efficiency-driven parsimony**, determining needle count within a single run.
4. Native support for **pullback ablations**, enabling multiple ablations at different depths along a single insertion via controlled retraction.
5. **Evaluation on 50 clinical hepatic cases** (94 targets, 3 difficulty tiers), combining quantitative metrics with expert review.

2 Method

2.1 Problem Formulation

Given T target tumor meshes $\{\mathcal{M}_t\}_{t=1}^{T}$, K obstacle meshes $\{\mathcal{O}_k\}_{k=1}^{K}$, and a skin surface $\mathcal{S}$, we seek a plan $\mathbf{P}$ optimizing four objectives f_1 to f_4. $\mathbf{P}$ contains an optimal number of needles N, and for each needle $i = 1, \ldots, N$, a tip position $\mathbf{p}_i \in \mathbb{R}^3$, an orientation (θ_i, ϕ_i) in spherical coordinates, and an ablation preset a_i. Each target is optimized independently and combined into a unified plan.

The four objectives reflect the placement criteria most commonly adopted in PTA decision-making:

$$f_1(\mathbf{P}) = \frac{n_{\mathrm{TP}}}{n_{\mathrm{TP}} + n_{\mathrm{FN}}} \qquad \text{(Coverage } \textit{or Sensitivity}\text{)} \tag{1}$$

$$f_2(\mathbf{P}) = \frac{n_{\mathrm{TP}}}{n_{\mathrm{TP}} + n_{\mathrm{FP}}} \qquad \text{(Efficiency } \textit{or Precision}\text{)} \tag{2}$$

$$f_3(\mathbf{P}) = \frac{\sum_i s_i \, e^{-k s_i}}{\sum_i e^{-k s_i}} \qquad \text{(Safety)} \tag{3}$$

$$f_4(\mathbf{P}) = 1 - \frac{1}{N} \sum_{i=1}^{N} \hat{d}_i^2 \qquad \text{(Depth)} \tag{4}$$

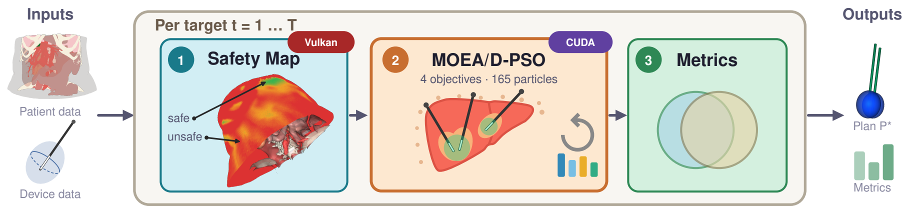

Fig. 1. Three-stage pipeline overview: (1) safety-map generation, (2) MOEA/D–PSO optimization, and (3) metrics computation against tumor and margin.

where $n_{\mathrm{TP}}/n_{\mathrm{FP}}/n_{\mathrm{FN}}$ are respectively the true positive, false positive, and false negative voxel counts sampled on a grid over the ablation and margin volumes, $s_i \in [0, 1]$ a per-trajectory safety, N the active needle count, and $\hat{d}_i$ the insertion depth, clamped to $[40, 200]$ mm and normalized to $[0, 1]$. Safety (3) uses a Boltzmann softmin ($k = 5$), ensuring the optimizer cannot hide one dangerous trajectory behind several safe ones. Needle parsimony is implicitly included in efficiency (2): in general additional needles add false positives (collateral damage), lowering this score. Coverage is evaluated against the MAM during optimization.

Our approach models this multi-needle planning problem as a *joint* multi-objective search, in which all needles associated with a given tumor are optimized simultaneously, rather than placed sequentially. To achieve this, we propose a pipeline in three stages (Fig. 1): (1) safety-map generation via Vulkan GPU fisheye rendering, (2) MOEA/D–PSO optimization with CUDA fitness evaluation, and (3) metrics computation.

2.2 Safety Map Generation

Safety is integrated in the optimization objective by pre-computing a dense safety map as a texture via GPU fisheye rendering (Fig. 2). Directions are sampled on

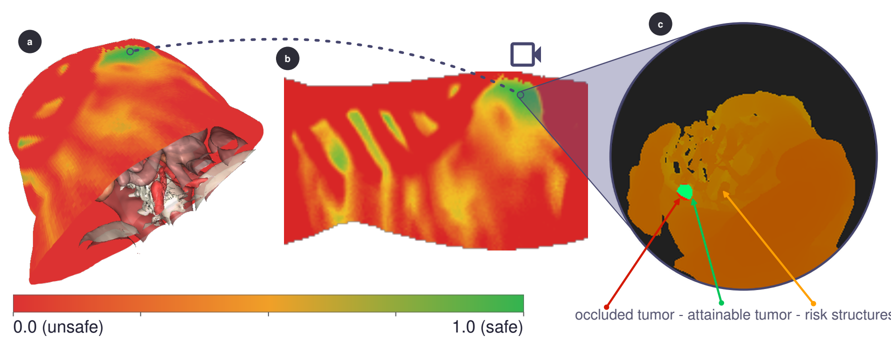

Fig. 2. **(a)** Safety map texture applied on the 3D mesh of the skin (color range from green=safe to red=unsafe). **(b)** Sphere safety map as a texture. **(c)** Occlusion rendering of anatomy and tumor from one specific entry point.

a 256×128 sphere texture. For each direction, a camera is placed on the skin surface looking inside the body and renders a 256^2 fisheye depth map in two passes: (1) obstacle MIN-blend and *back-face* target MAX-blend, yielding safety as the unoccluded target ratio; (2) liver-margin clearance ($<$10 mm discarded). Validated points are indexed in a 32×16-bin spherical grid for $O(1)$ lookup. The map is computed once per case before optimization and remains static throughout the search, with needle safety queried per-particle by a single texture fetch during GPU fitness evaluation.

2.3 MOEA/D–PSO Optimization

With four competing objectives, dominance-based algorithms such as NSGA-II suffer from weak selection pressure in high-dimensional objective spaces [29]. We adopted a Multiobjective Evolutionary Algorithm based on Decomposition (MOEA/D) [29] with Particle Swarm Optimization (PSO) as the search operator. While decomposition-based multi-objective PSO has been explored previously in other contexts [28,1], our contributions lie in the clinical planning formulation and domain-specific operators described below.

PSO is a population-based search method in which candidate solutions ("particles") iteratively move through the decision space by combining their own momentum with attraction toward known good positions. Rather than comparing solutions via dominance, MOEA/D decomposes the 4-objective problem into N_w scalar sub-problems, each defined by a *weight vector* $\boldsymbol{\lambda} = (\lambda_1, \ldots, \lambda_4)$ that assigns a different relative priority to the four objectives ($\lambda_i \geq 0$, $\sum_i \lambda_i = 1$). Das–Dennis vectors [7] distribute these weights uniformly on the 4-simplex by discretizing each component into multiples of $1/H$; with granularity $H = 8$ this yields $N_w = \binom{4+H-1}{H} = 165$ vectors, each defining one sub-problem optimized by a dedicated particle. Boundary vectors are added to better cover extreme Pareto regions (e.g. pure coverage or pure safety).

Each sub-problem converts its 4-objective evaluation into a single scalar via Penalty-based Boundary Intersection (PBI) scalarization [29]: $g^{\mathrm{PBI}} = d_1 + \vartheta \cdot d_2$, where d_1 is the projection of the objective vector onto the weight direction (measuring *convergence* toward the ideal point $\mathbf{z}^*$) and d_2 is the perpendicular distance from that direction (penalizing deviation from the assigned trade-off). The ideal point $\mathbf{z}^* = (z_1^*, \ldots, z_4^*)$ tracks the best value found so far and is updated every iteration. We set $\vartheta = 5.0$, providing strong diversity pressure to prevent sub-problems from collapsing on the same region of the Pareto front [29]. Particle velocity is updated via the Clerc–Kennedy constriction rule [5]: $\mathbf{v}_{t+1} = \chi(\mathbf{v}_t + c_1 r_1(\mathbf{p}_{\text{best}} - \mathbf{x}_t) + c_2 r_2(\mathbf{g}_{\text{best}} - \mathbf{x}_t))$, with $c_1 = c_2 = 2.05$ and $\chi \approx 0.7298$, ensuring stable convergence without inertia tuning.

Each particle encodes a plan as a vector with 12 variables per needle: direction (θ, ϕ) in spherical coordinates, tip position (p^x, p^y, p^z), primary burn size scalar $s \in [0, 1]$ (mapped to ellipsoid dimensions via manufacturer-calibrated profiles), number of burns $n \in 1, 2, 3$ along the direction of the needles to allow for pullback ablation strategies, pullback spacings δ^j, per-burn sizes s^j, and activation a (≥ 0.5: active, otherwise suppressed). Total dimensionality is $N_{\max} \times 12$, with

$N_{\max}$ the maximum number of needles allowed. The *needle tip* is the decision variable anchor; the ablation epicenter is derived as $\mathbf{e} = \mathbf{p} - \hat{\mathbf{d}} \cdot \delta_{\text{offset}}$, and pullback burns are positioned along the shaft at $\mathbf{c}_j = \mathbf{e} + \hat{\mathbf{d}} \cdot \sum_{k=1}^{j} \delta^k$.

Each particle maintains $T_n = 20$ weight-vector neighbors; $\mathbf{g}_{\text{best}}$ is the best-PBI particle among the T_n neighbors, with $n_r = 2$ replacements per iteration. Domain-aware continuous mutations (direction rotation up to π rad, position $\pm15\%$, size $\pm20\%$; probability 0.1 per needle) and needle-level crossover (every 7 iterations) preserve geometric structure. Discrete structural mutations (add/remove/replace, every 13 iterations) enable variable needle count. Optimization terminates via multi-criteria early stopping: all four objectives must individually stagnate ($<0.1\%$ improvement over 100 iterations) after a 25% grace period, confirmed over 5 consecutive checks.

2.4 GPU Fitness Evaluation

The evaluation of N_w candidate plans per iteration, each requiring volumetric coverage assessment, constitutes a computational bottleneck. We accelerated this with CUDA, using a signed distance field (SDF) at $\sim$2 mm resolution uploaded as a 3D texture for mesh-accurate containment queries via trilinear interpolation. A single kernel evaluates all particles in parallel: needle ellipsoids are decoded into shared memory, the tight union bounding box is sampled on an adaptive grid and each point is tested for ellipsoid and target membership. To avoid local recurrence, full coverage of a MAM of at least $+\delta = 5$ mm from the tumor surface is mandatory [11,25]. However, in practice, the multi-objective optimization tends to produce ablations that conform too tightly to the MAM surface, occasionally leaving irregular parts of the margin under-covered. To guarantee full margin coverage, we chose to inflate δ by an additional 3 mm during optimization. Values for $n_{\text{TP}}/n_{\text{FP}}/n_{\text{FN}}$ are accumulated via shared-memory reduction. Safety is evaluated by associating each needle's position and direction to the corresponding insertion point on the safety map.

Prior methods fixed needle count *a priori* or estimated it from volumetric ratios before optimization [16,13,14], committing structural decisions before the full plan is known. In our approach, all $N_{\max}$ needles are encoded in every particle; the activation variable determines which are active ($a_i \geq 0.5$). The optimizer selects the appropriate count: adding a superfluous needle increases false positives, lowering efficiency (2), while discrete mutations (add/remove/replace) explore different counts across the Pareto front.

3 Dataset and Metrics

The dataset used in this study was built from the Colorectal-Liver-Metastases (CRLM) database of pre-segmented images [26]. Filters were used to select cases as per the COLLISION classification of ablability [12]: Tier 1 has single tumors with simple access and lowest risk; Tier 2 includes intermediate cases with either multiple lesions or bilobar distribution; Tier 3 contains multi-lesion and bilobar tumors, with the highest planning complexity. A total of 50 cases, comprising 94 individual tumors, was selected by an expert clinician among cases with no extrahepatic disease and maximal tumor diameter ≤ 4.3 cm, with the following distribution: Tier 1: 25 cases (50%), Tier 2: 15 cases (30%), Tier 3: 10 cases (20%). Mean tumor diameter was 12.0 ± 6.6 mm. The average distance to the closest critical structure across tumors was 4.8 ± 4.4 mm, hepatic vessels (hepatic veins, portal vein, inferior vena cava) being the nearest obstacle in 64% of cases. In 59% of cases, the tumor was located < 5 mm from the liver surface, requiring angled insertions through parenchyma before reaching the tumor. Mean distance to the skin surface was 54.3 ± 25.3 mm, reflecting the range of insertion depths encountered in clinical practice.

For each case, all segmented structures (liver, tumors, vasculature, skin, and 15 organs) were reconstructed as 3D surface meshes. A manual plan was created by a hepato-biliary surgeon under clinical routine conditions, placing needles interactively on 2D slices using Medtronic Emprint microwave presets identical to those available to the auto-planner. The full dataset has been made publicly available at: https://figshare.com/s/13c01677c744eb1625c6.

Because our optimizer aims to cover the MAM, we computed metrics mostly against the margin. Coverage, efficiency, and Dice similarity coefficient (DSC) quantify the voxel overlap between the ablation zone and the margin volume. All overlap metrics were computed at 0.5 mm isotropic resolution. The 95th-percentile Hausdorff distance (HD95), less sensitive to outliers than the full Hausdorff distance, measures boundary agreement. We additionally computed the distance from needle to closest critical structure (DTC, in mm), a standard safety metric [24,13] and the average needle insertion depth (mm). Finally, Cohen's d and q-value were computed to evaluate significance of the results.

To complement quantitative metrics, the same surgeon-scientist independently reviewed all 94 auto-planner targetsand assessed: (1) *Acceptability* on a 5-point Likert scale (1=unacceptable, 2=major changes needed, 3=minor changes needed, 4=minor optional, 5=fully acceptable), and (2) *Preference*, indicating which plan they would follow clinically (Auto-planner, Expert or Either). Free-text comments were collected to identify recurring clinical concerns and planning biases.

4 Experiments and Results

All experiments were run on a dedicated workstation equipped with an Intel Core i9 processor, 32.0 GiB of RAM, and an NVIDIA RTX 4080 SUPER graphics processing unit. Median per-target optimization time was 5.2 s (mean 5.4 s), with a one-time safety map pre-computation of 2.8 s per case.

Table 1 shows paired results. The auto-planner achieved full MAM coverage in 100% of cases, significantly improving DSC (0.892 vs. 0.525), and maintaining wider safety margins (DTC 6.0 vs. 4.4 mm) (Fig. 3B). Efficiency shows that expert plans caused ∼61% collateral damage on healthy tissue vs. ∼17% for

Table 1. Per-case comparison between automatic and expert planning averaged over 94 targets from 50 cases: Average (SD) are reported with difference (Δ) and statistical significance (Wilcoxon signed-rank test, Benjamini–Hochberg FDR correction).

Structure	Metric	Auto	Expert	Δ	Cohen's d	q-value
Target	Coverage	**1.000** (0.000)	0.988 (0.038)	+0.012	0.31	0.003
	Coverage	**1.000** (0.000)	0.939 (0.100)	+0.061	0.61	<0.001
Margin	Efficiency	**0.829** (0.067)	0.394 (0.159)	+0.435	3.00	<0.001
	DSC	**0.892** (0.040)	0.525 (0.145)	+0.366	2.75	<0.001
	DTC (mm)	**6.0** (3.1)	4.4 (2.8)	+1.6	0.51	<0.001
	Depth (mm)	102.5 (23.3)	**98.0** (20.5)	+4.5	0.20	0.214
	HD95 (mm)	**5.9** (1.0)	9.1 (2.6)	−3.2	−1.23	<0.001

the auto-planner. Both methods provided comparable insertion depth (102.5 vs. 98.0 mm, $q = 0.214$), indicating equivalent complexity of execution.

The difference between methods increased with case difficulty (Fig. 3A). Expert DSC dropped from 0.578 on Tier 1 to 0.450–0.464 in Tiers 2–3, while the auto-planner maintained DSC at 0.899, 0.875, and 0.898. Expert efficiency declined from 0.445 (Tier 1) to 0.314–0.336 in complex cases (Fig. 4), whereas the auto-planner maintained conformal plans regardless of target count. The auto-planner achieved consistently lower HD95 (Fig. 3C) suggesting better centering of ablations and less over-treatment. Figure 4 shows representative plans across tiers. Auto-planned ablation zones conform more closely to the margin boundary while expert plans show over-ablation, particularly in multi-target cases.

The expert clinical review yielded a mean acceptability of 4.4 ± 0.8 across all 94 targets: 88% scored ≥ 4 (acceptable with at most minor optional improvements) and 99% scored ≥ 3 (minor changes at most). The auto-planner was preferred in 87% of targets, while 10% were rated as equivalent, the expert plan being preferred in only 3%. Acceptability remained stable across tiers (Tier 1: 4.4 ± 0.9, Tier 2: 4.5 ± 0.7, Tier 3: 4.5 ± 0.7), confirming that clinical quality did

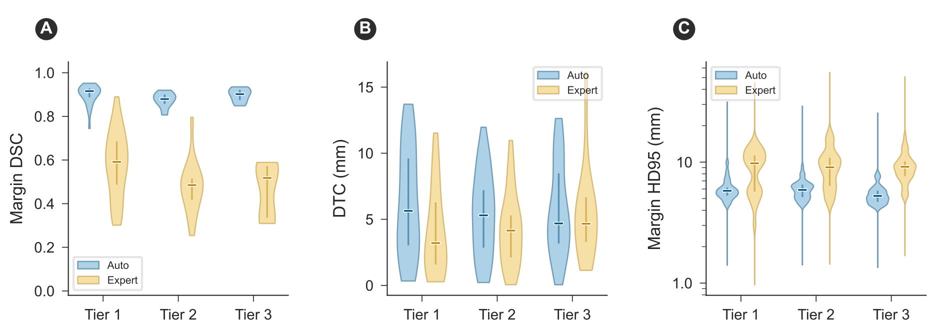

Fig. 3. Quantitative results per tier: **(A)** Margin DSC, **(B)** DTC, **(C)** Margin HD95.

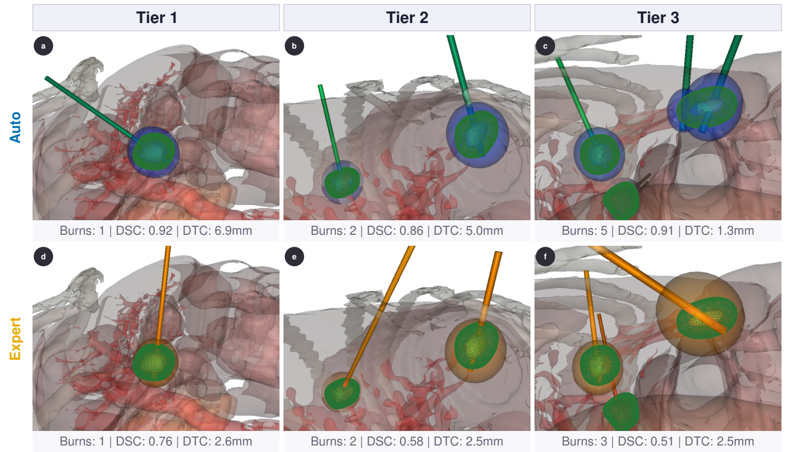

Fig. 4. Qualitative comparison across tiers. Top: auto-planner; bottom: expert. Tumors and margins (green), ablation zones and needles (blue/yellow), translucent organs.

not degrade with case complexity. The most frequent reason for preferring the auto-planner was inadequate coverage of the margin in the expert plan, explicitly noted in 40% of targets, underlining both the difficulty of planning manually from 2D slices and the importance of a full MAM coverage.

Recurrent concerns included trajectories leaving the liver (10%), superfluous applicators (13%), and overly tangential approaches (7%), suggesting future constraints on intrahepatic path length and entry angle. The reviewer also noted cognitive biases in manual plans (*in-plane trajectory bias*, *landmark bias*), highlighting the value of automated planning.

5 Conclusion

We presented a GPU-accelerated pipeline that jointly optimizes multi-needle placement, ablation parameters, and trajectory safety for percutaneous thermal ablation. A 4-objective MOEA/D–PSO formulation with per-needle activation encoding determines needle configurations and count in a median of 5.2 s per target without sequential commitment of individual needles.

On 50 paired clinical hepatic cases, the auto-planner improves on almost all metrics compared to the expert. Multi-target planning, where clinicians must mentally coordinate high-dimensional trade-offs, is where the method offers the largest measured improvement. An expert review confirmed clinical acceptability with minor or no adjustments in 99% of cases (single-reviewer assessment; multi-reader validation remains future work). A few outliers remain, indicating potential gains from added constraints suggested through the questionnaire, or multi-run selection. To get even closer to the perfect burn, in future work we intend to integrate our fast physics-based ablation zone simulations [19,18], that account for multi-needle thermal interaction effects where overlapping zones are not simply additive.

Acknowledgments. This work of the Interdisciplinary Thematic Institute HealthTech, as part of the ITI 2021-2028 program of the University of Strasbourg, CNRS and Inserm, was supported by IdEx Unistra (ANR-10-IDEX-0002) and SFRI (STRAT'US project, ANR-20-SFRI-0012) under the framework of the French Investments for the Future Program. It has been partially funded under the framework of the French Investments for the Future Program, by French state funds managed within the "Plan Investissements d'Avenir", by the ANR (reference ANR-10-IAHU-02).

Disclosure of Interests. The authors have no conflict of interest to declare.

References

1. Al Moubayed, N., Petrovski, A., McCall, J.: D2MOPSO: MOPSO based on decomposition and dominance with archiving using crowding distance in objective and solution spaces. Evolutionary Computation **22**(1), 47–77 (2014). https://doi.org/10.1162/EVCO_a_00104
2. Baegert, C., Villard, C., Schreck, P., Soler, L., Gangi, A.: Trajectory optimization for the planning of percutaneous radiofrequency ablation of hepatic tumors. Computer Aided Surgery **12**(2), 82–90 (2007). https://doi.org/10.3109/10929080701312000
3. Butz, T., Warfield, S.K., Tuncali, K., Silverman, S.G., van Sonnenberg, E., Jolesz, F.A., Kikinis, R.: Pre- and intra-operative planning and simulation of percutaneous tumor ablation. In: Proceedings of MICCAI 2000. LNCS, vol. 1935, pp. 317–326. Springer (2000). https://doi.org/10.1007/978-3-540-40899-4_32
4. Chaitanya, K., Audigier, C., Balascuta, L.E., Mansi, T.: Automatic planning of liver tumor thermal ablation using deep reinforcement learning. In: Proceedings of MIDL 2022. PMLR, vol. 172, pp. 219–230 (2022)
5. Clerc, M., Kennedy, J.: The particle swarm – explosion, stability, and convergence in a multidimensional complex space. IEEE Transactions on Evolutionary Computation **6**(1), 58–73 (2002). https://doi.org/10.1109/4235.985692
6. Crocetti, L., de Baere, T., Pereira, P.L., Tarantino, F.P.: CIRSE standards of practice on thermal ablation of liver tumours. CardioVascular and Interventional Radiology **43**, 951–962 (2020). https://doi.org/10.1007/s00270-020-02471-z
7. Das, I., Dennis, J.E.: Normal-boundary intersection: A new method for generating the Pareto surface in nonlinear multicriteria optimization problems. SIAM Journal on Optimization **8**(3), 631–657 (1998). https://doi.org/10.1137/S1052623496307510
8. Ding, F., Wu, W., Jiang, W., Zhou, Z., Wu, S.: Computer-assisted treatment planning and mathematical modeling for percutaneous liver tumor ablation: An updated survey. Annals of Biomedical Engineering (2025). https://doi.org/10.1007/s10439-025-03850-8
9. Galle, P.R., Forner, A., Llovet, J.M., Mazzaferro, V., Piscaglia, F., Raoul, J.L., Schirmacher, P., Vilgrain, V.: EASL clinical practice guidelines: Management of hepatocellular carcinoma. Journal of Hepatology **69**(1), 182–236 (2018). https://doi.org/10.1016/j.jhep.2018.03.019

10. Hamzé, N., Voirin, J., Collet, P., Jannin, P., Haegelen, C., Essert, C.: Pareto front vs. weighted sum for automatic trajectory planning of deep brain stimulation. In: Proceedings of MICCAI 2016. pp. 534–541. Springer (2016)
11. Laimer, G., Schullian, P., Jaschke, N., Putzer, D., Eberle, G., Alzaga, A., Odisio, B., Bale, R.: Minimal ablative margin (MAM) assessment with image fusion: an independent predictor for local tumor progression in hepatocellular carcinoma after stereotactic radiofrequency ablation. European Radiology **30**(5), 2463–2472 (2020). https://doi.org/10.1007/s00330-019-06609-7
12. Lei, S.v.d., Puijk, R.S., et al.: Thermal ablation versus surgical resection of small-size colorectal liver metastases (COLLISION): an international, randomised, controlled, phase 3 non-inferiority trial. The Lancet Oncology **26**(2), 187–199 (2025). https://doi.org/10.1016/S1470-2045(24)00660-0
13. Li, J., Xu, Y., Shen, N., Feng, L., Ran, Z., Deng, Z.: A practical pretreatment planning method of multiple puncturing for thermal ablation surgery. Biocybern Biomed Eng **40**(4), 1469–1485 (2020). https://doi.org/10.1016/j.bbe.2020.08.004
14. Li, S., Zhou, F., Zhang, Y., Xu, S., Wang, Y., Cheng, L., Bie, Z., Li, B., Li, X.G.: Multi-stage automatic and rapid ablation and needle trajectory planning method for CT-guided percutaneous liver tumor ablation. Medical Physics **52**(1), 113–130 (2025). https://doi.org/10.1002/mp.17450
15. Liang, L., Cool, D., Kakani, N., Wang, G., Ding, H., Fenster, A.: Automatic radiofrequency ablation planning for liver tumors with multiple constraints based on set covering. IEEE Transactions on Medical Imaging **39**(5), 1459–1471 (2020). https://doi.org/10.1109/TMI.2019.2950947
16. Liu, S., Xia, Z., Liu, J., Xu, J., Ren, H., Lu, T., Yang, X.: Automatic multiple-needle surgical planning of robotic-assisted microwave coagulation in large liver tumor therapy. PLOS ONE **11**(3), e0149482 (2016). https://doi.org/10.1371/journal.pone.0149482
17. Lukes, A., Bale, R., Freysinger, W.: Automatic trajectory planning for stereotactic radiofrequency ablation in non-discrete search space. IJCARS **20**, 1349–1360 (2025). https://doi.org/10.1007/s11548-025-03386-1
18. Mehtali, J., Verde, J.M., Essert, C.: C-NCA: Chained neural cellular automata for fast and accurate thermal ablation estimation. In: Proceedings of MICCAI 2025. pp. 67–77. LNCS, Springer (2025). https://doi.org/10.1007/978-3-032-04965-0_7
19. Mehtali, J., Verde, J.M., Essert, C.: HEAT: High-efficiency simulation for thermal ablation therapy. International Journal of Computer Assisted Radiology and Surgery **20**(6), 1135–1143 (2025). https://doi.org/10.1007/s11548-025-03350-z
20. Meister, F., Audigier, C., Passerini, T., Lluch, É., Mihalef, V., Maier, A., Mansi, T.: Fast automatic liver tumor radiofrequency ablation planning via learned physics model. In: Proceedings of MICCAI 2022. LNCS, vol. 13437, pp. 167–176. Springer (2022). https://doi.org/10.1007/978-3-031-16449-1_17
21. Pan, K., Qin, J., Qin, G.: A rapid path planning approach for liver tumor ablation with comprehensive constraints. BMC Medical Imaging **26**, 73 (2026). https://doi.org/10.1186/s12880-025-02120-2
22. Schumann, C., Rieder, C., Haase, S., Teichert, K., Süss, P., Isfort, P., Bruners, P., Preusser, T.: Interactive multi-criteria planning for radiofrequency ablation. IJCARS **10**(6), 879–889 (2015). https://doi.org/10.1007/s11548-015-1201-6
23. Scorza, D., El Hadji, S., Cortés, C., Bertelsen, Á., Cardinale, F., Baselli, G., Essert, C., De Momi, E.: Surgical planning assistance in keyhole and percutaneous surgery: A systematic review. Medical Image Analysis **67**, 101820 (2021). https://doi.org/10.1016/j.media.2020.101820

24. Seitel, A., Engel, M., Sommer, C.M., Radeleff, B.A., Essert-Villard, C., et al.: Computer-assisted trajectory planning for percutaneous needle insertions. Medical Physics **38**(6), 3246–3259 (2011). https://doi.org/10.1118/1.3590374
25. Shady, W., Petre, E.N., Gonen, M., Erinjeri, J.P., Brown, K.T., et al.: Percutaneous radiofrequency ablation of colorectal cancer liver metastases: Factors affecting outcomes—a 10-year experience at a single center. Radiology **278**(2), 601–611 (2016). https://doi.org/10.1148/radiol.2015142489
26. Simpson, A.L., Peoples, J., Creasy, J.M., Fichtinger, G., et al.: Preoperative CT and survival data for patients undergoing resection of colorectal liver metastases. Scientific Data **11**(1), 172 (Feb 2024). https://doi.org/10.1038/s41597-024-02981-2
27. Westby, K., Westby, D., McKevitt, K., Moloney, B.M.: Artificial intelligence in thermal ablation: Current applications and future directions in microwave technologies. Biomimetics **10**(12), 818 (2025). https://doi.org/10.3390/biomimetics10120818
28. Zapotecas Martínez, S., Coello Coello, C.A.: A multi-objective particle swarm optimizer based on decomposition. In: Proceedings of GECCO 2011. pp. 69–76. ACM (2011). https://doi.org/10.1145/2001576.2001587
29. Zhang, Q., Li, H.: MOEA/D: A multiobjective evolutionary algorithm based on decomposition. IEEE Transactions on Evolutionary Computation **11**(6), 712–731 (2007). https://doi.org/10.1109/TEVC.2007.892759